

26 **Abstract**

27 Identification of induced pluripotent stem (iPS) progenitor cells, the iPS forming cells in early
28 stage of reprogramming, could provide valuable information for studying the origin and
29 underlying mechanism of iPS cells. However, it is very difficult to identify experimentally
30 since there are no biomarkers known for early progenitor cells, and only about 6 days after
31 reprogramming initiation, iPS cells can be experimentally determined via fluorescent probes.
32 What is more, the ratio of progenitor cells during early reprogramming period is below 5%,
33 which is too low to capture experimentally in the early stage.

34 In this paper, we propose a novel computational approach for the identification of iPS
35 progenitor cells based on machine learning and microscopic image analysis. Firstly, we
36 record the reprogramming process using a live cell imaging system after 48 hours of infection
37 with retroviruses expressing Oct4, Sox2 and Klf4, later iPS progenitor cells and normal
38 murine embryonic fibroblasts (MEFs) within 3 to 5 days after infection are labeled by
39 retrospectively tracing the time-lapse microscopic image. We then calculate 11 types of cell
40 morphological and motion features such as area, speed, etc., and select best time windows for
41 modeling and perform feature selection. Finally, a prediction model using XGBoost is built
42 based on the selected six types of features and best time windows. Our model allows several
43 missing values/frames in the sample datasets, thus it is applicable to a wide range of
44 scenarios.

45 Cross-validation, holdout validation and independent test experiments showed that the
46 minimum precision is above 52%, that is, the ratio of predicted progenitor cells within 3 to 5
47 days after viral infection is above 52%. The results also confirmed that the morphology and

48 motion pattern of iPS progenitor cells is different from that of normal MEFs, which helps
49 with the machine learning methods for iPS progenitor cell identification.

50

51 **Keywords**

52 iPS progenitor cell; Machine learning; XGBoost; Cell reprogramming; Morphology features

53

54 **Author Summary**

55 Identification of induced pluripotent stem (iPS) progenitor cells could provide valuable
56 information for studying the origin and underlying mechanism of iPS cells. However, it is
57 very difficult to identify experimentally since there are no biomarkers known for early
58 progenitor cells, and only after about 6 days of induction, iPS cells can be experimentally
59 determined via fluorescent probes. What is more, the percentage of the progenitor cells during
60 the early induction period is below 5%, too low to capture experimentally in early stage. In
61 this work, we proposed an approach for the identification of iPS progenitor cells, the iPS
62 forming cells, based on machine learning and microscopic image analysis. The aim is to help
63 biologists to enrich iPS progenitor cells during the early stage of induction, which allows
64 experimentalists to select iPS progenitor cells with much higher probability, and furthermore
65 to study the biomarkers which trigger the reprogramming process.

67 **Introduction**

68 Induced pluripotent stem (iPS) cells are cells with embryonic-like state reprogrammed
69 from mouse embryonic or adult fibroblasts by introducing the defined factors[1]. Since
70 Takahashi and Yamanaka[1] first proposed the methods of reprogramming somatic cells to
71 iPS cells, it has become an important method for clinical cell therapy, and revolutionized
72 regenerative medicine[2], such as platelet deficiency[3], spinal cord injury[4], macular
73 degeneration[5], Parkinson's disease[6] and Alzheimer's disease[7]. However, obstacles still
74 remain in scientific and clinical applications for iPS cells because of potential tumorigenicity
75 and low efficiency of reprogramming technique[8-10]. Tumorigenicity is attributed to the
76 introduction of tumorigenic factors such as Oct4, Sox2, Klf4 and c-Myc, of which
77 over-expression is generally associated with tumors. Inefficiency concerns low frequency for
78 reprogramming cells, which is less than a small proportion of 5%. In some induction
79 protocols, the ratio of progenitor cells during the early stage of reprogramming is even under
80 0.5%.

81 The above-mentioned obstacles are mainly due to poor understanding of molecular
82 mechanisms in iPS cell reprogramming, which ultimately prevented this technology from a
83 wide range of scientific and clinical applications. Theoretical mechanisms models are
84 proposed such as two-step process model[11] and seesaw model[12], most of which focus on
85 how factors such as Oct4, Sox2, Klf4, and c-Myc induce pluripotency. Experimental
86 approaches based on epigenetic profiling, RNA screening or single-cell analysis for
87 uncovering the mechanisms are limited by the low reprogramming efficiency or the lack of
88 biomarkers for progenitor cells [13-20].

89 Recent studies found that iPS progenitor cells differed from normal MEFs in
90 morphology, motion or proliferation rate. Smith et al.[21] found that iPS progenitor cells
91 showed smaller cellular area and higher proliferative rate than normal MEFs via time-lapse
92 imaging. Zhang et al.[22] also found that iPS cells exhibited distinct morphology features and
93 different proliferative rate comparing with larger and quiescent differentiated cells. Li et al.
94 [23] showed the mesenchymal-to-epithelial transition, a process with significant
95 morphological changes, was a key cellular mechanism for induced pluripotency. Megyola et
96 al.[24] demonstrated that migratory motions for progenitor cells were often distinct in
97 direction and distance to bring distant progenitor cells together. Most of these studies relied
98 on time-lapse microscopy, which allowed studying/tracing cellular events in early
99 reprogramming by direct observation [24]. Since iPS progenitor cells exhibit unique
100 morphology and motion features, computational methods, especially machine learning based
101 methods, could provide an alternative method to identify iPS progenitor cells in the early
102 stage of reprogramming process through learning the morphology and motion patterns of iPS
103 progenitor cells.

104 Usually cell detection, segmentation and tracking are firstly required for computational
105 methods to study cell images. Li et al.[25] proposed DCELLIQ for cell nuclei tracking based
106 on neighboring graph and integer programming technique. Dzyubachyk et al.[26] relied on
107 coupled active surfaces algorithm for cell segmentation and tracking in time-lapse
108 fluorescence microscopy images. Maška et al.[27] presented a tracking method for fluorescent
109 cells based on coherence-enhancing diffusion filtering and Chan-Vese model. Türetken et
110 al.[28] proposed an integer programming approach for tracking elliptical cell populations in

111 time-lapse image sequences. Payer et al.[29] developed a recurrent fully convolutional
112 network architecture for instance segmentation and tracking with training network using an
113 embedding loss based on cosine similarities.

114 Recently machine learning/deep learning methods have been extensively developed for
115 the prediction and study of cell images. Using cell images, Erdmann et al.[30] introduced a
116 machine learning based framework for image-based screen analysis. Valen et al.[31] tried to
117 solve cell image segmentation problem utilizing deep convolutional neural networks, and
118 demonstrated its effectiveness in segmenting fluorescent images of cell nuclei. Chen et al.[32]
119 achieved high classification accuracy in label-free white blood T-cells against colon cancer
120 cell via a deep learning method. Similarly with a deep convolutional neural network method,
121 Kraus et al.[33] analyzed the microscopic images for yeast cell and other pheromone-arrested
122 cells, and Gao et al.[34] achieved a high ranking in the human epithelial-2 cell image
123 classification competition hosted by ICPR2014. Together with principal component analysis,
124 machine learning method can be used to infer regulatory network patterns underlying stem
125 cell pluripotency[35]. The ability of machine learning has been demonstrated with its
126 extensive application for cellular image data, however, it has been seldom used in the
127 identification of iPS progenitor cells in the early stage.

128 In this article, we propose a machine learning based approach to detect iPS progenitor
129 cells during the early stage of reprogramming. Given the cell images recorded via live-cell
130 imaging system during the reprogramming process, the paper aims to identify iPS progenitor
131 cells against normal MEFs in the same stage. Since the iPS progenitor cell to normal MEFs
132 ratio is usually below 5%, this makes the identification problem very difficult. In the paper we

133 use Imaris, a software from Bitplane, to analyze and process microscopic cell images from
134 live-cell imaging system. Surpass, a module of Imaris is then used to extract cell numerical
135 information in the same time period. We then develop a machine learning method for
136 identification of iPS progenitor cells based on the extracted morphological and motional
137 features. The prediction model is built with XGBoost based on the selected six types of
138 features and time windows. In our method, cell division is not considered, and frames
139 contained in selected time windows are uniform. The model performance is evaluated by
140 three different validation methods. When tested on labeled datasets with a ratio of about 1:5
141 between progenitor cells and normal MEFs, the prediction precision to identify iPS progenitor
142 cells is above 52% during the first 1-3 days of reprogramming after adding iCD1 medium.
143 The image-based machine learning method allows experimentalists to select iPS progenitor
144 cells with much higher probability, and furthermore to study the biomarkers which trigger the
145 reprogramming process.

146

147 **Materials and Methods**

148 The workflow used in the paper is presented in **Fig 1**, which mainly includes feature
149 extraction, preprocessing with missing values, feature selection, machine learning for training
150 and validation. In this workflow, we acquire time-lapse images through experiments firstly,
151 then we label iPS progenitor cells and normal MEFs manually to generate datasets by tracing
152 images retrospectively. Next, we generate 11 types of morphology and motion features with
153 Imaris software. After the feature extraction, we perform time window selection and a
154 two-step feature selection. Finally, we build the prediction model based on the selected six

155 types of features and six time windows. The machine learning algorithm for modeling is
156 XGBoost, a gradient boosting tree[36]. In the following sections, we will describe the steps of
157 our model in detail.

158 **Fig 1. Flow chart of the machine learning based approach for iPS progenitor cell** 159 **identification**

160 In time-lapse imaging, we record the reprogramming process periodically among 54 fields
161 after 48h of viral infection. For retrospective labeling, the figure only shows the labeled cell
162 images of the first frame of all eight phases. Only datasets from phase 1, 2 and 3 are used for
163 model training and testing.

164

165 **Cell culture and generation of iPS cells**

166 Mouse embryonic fibroblasts (MEFs) are derived from E13.5 embryos carrying the Oct4
167 promoter-driven GFP reporter gene[37] and maintain in DMEM (HyClone) supplemented
168 with 10% FBS (Gibco). To generate iPS cells, MEFs within two passages are seeded at a
169 density of 5×10^4 cells/well in 6-well plates and cultured overnight. The next day, MEFs are
170 infected with retroviral supernatants containing the DsRed gene and three reprogramming
171 factors (Oct4, Sox2, Klf4) twice in a 48h process. After 48h of infection, iCD1 medium[38] is
172 changed every day to achieve high reprogramming efficiency. iPS cell colonies are obtained
173 5-7 days post-treatment in iCD1 based on the Oct4-GFP expression.

174

175 **Time-lapse imaging**

176 Reprogramming process is recorded using an Olympus IX81 live cell imaging system

177 equipped with a 10× UPlanFL objective, iXon3 EMCCD Camera. The date on which viral
178 supernatants are removed and iCD1 medium are added is defined as Day 0. From Day 0,
179 MEFs images are taken for a total time of 135 hours and 40 minutes. For the first 48 hours
180 and 40 minutes, both bright-field and red fluorescence images are acquired at 10-minute
181 intervals. After two days of the dual-channel imaging, a green fluorescence channel is added
182 to indicate the expression of Oct4-GFP and acquisition intervals are adjusted to 30 minutes.
183 Motorized Stage Control is used to follow cells in the same field and a total of 54 fields are
184 selected at each time for further analysis.

185 Cell images taken within the first 48 hours and 40 minutes since Day 0 are used to
186 construct the dataset because after this time the Oct4-GFP is added to identify the progenitor
187 cells experimentally and the paper tries to identify/predict progenitor cells using
188 computational methods as early as possible.

189

190 **Cell segmentation and numerical feature extraction**

191 The original files are time-lapse microscope images in TIFF format, whose pixels are
192 770 * 746 and the actual size is 1000 microns * 967 microns. Because some fields do not
193 show distinct Oct4-GFP signals and result in no signals for iPS cells in these fields, we only
194 use images from 33 fields for modeling. Imaris (Version 7) software is used to segment cells
195 in the images of these 33 fields and extract the corresponding numerical features for the
196 segmented cells. During this process, the parameter values of cell and nucleus intensity are set
197 the same for all the cells in each field, and cell tracking duration parameter of greater than
198 5000s is used. Imaris utilizes red fluorescent channel for cell segmentation and tracking. The

199 image segmentation is based on the Watershed Algorithm, which is very sensitive to weak
200 edges and intensity in images.

201 Features are computed for each segmented/identified cell image at different time frames
202 by Imaris, and these features denote the morphological and movement information of the
203 segmented cells during reprogramming. Overall 11 types of features are extracted (volume,
204 area, sphericity, ellipsoid-prolate, ellipsoid-oblate, nucleus-cytoplasm volume ratio,
205 displacement, speed, Intensity-stdDev, Intensity-Max, Intensity-Min) and each type contains
206 features in several frames of the selected uniform time windows. The detailed list of features
207 is presented in Part 1 of the **S1 File**.

208

209 **Cell image dataset generation**

210 Cell image datasets for machine learning consist of normal MEFs cell images and
211 progenitor cell images within the first 48 hours and 40 minutes. The datasets will be used by
212 our machine learning method in the training and testing processes.

213 At first, we manually label iPS progenitor cell and normal MEFs cell images identified
214 by Imaris software within the first 48 hours and 40 minutes. Experimentally iPS cells can be
215 determined only by Oct4-GFP expression signal, which cannot be observed until the seventh
216 day after transfection with Yamanaka's factors. Cells showing green fluorescence in images
217 are considered as iPS cells. We can then label iPS progenitor cells in the early reprogramming
218 process by cell image backtracking. The corresponding cell images are retrospectively traced
219 frame by frame from GFP expression to the first 48 hours and 40 minutes (**Fig 1**). Due to
220 three one-hour iCD1 medium changes, the total reprogramming period is divided into four

221 periods, the first period is 16 hours and 50 minutes long, from 18 hours to 24 hours and 40
222 minutes denoted as phase 1 in the paper, the second from 25 hours and 50 minutes to 40 hours
223 and 40 minutes denoted as phase 2, and the third from 41 hours and 50 minutes to 48 hours
224 and 40 minutes denoted as phase 3. In this paper, we focus on these three periods (phases 1, 2
225 and 3) only because of tiny ratio for iPS progenitor cells in the first 16 hours and 50 minutes,
226 which is even less than 2%.

227 Two rules are applied in the paper for generating the cell image datasets, (1) cell division
228 is not considered; (2) frames from the same window of each phase are selected for modeling
229 among uniform time periods. When cell division is taken into account, features in the mother
230 cell and its daughter cells are not comparable, for example, the area of mother cell is much
231 bigger than that of its daughter cells, thus the machine learning model will fail to process this
232 cell. The second rule guarantees that time dimension (time period and length) for the cell
233 image data samples should be uniform.

234 For each cell, not every image in different frames can be identified by Imaris due to the
235 fact that different parameter settings (cell or nucleus intensity threshold, cell tracking duration)
236 by Imaris will lead to different segmented cell images in a frame. This results in cell image
237 data missing in some frames, thus our method allows a certain number of missing cell images
238 in the selected uniform time periods and tries to find the maximum number of continuous
239 cells images in this uniform time period.

240 Overall three cell image sets are generated for three phases, each with an approximately
241 1:5 ratio between progenitor cell images and normal MEFs cell images. For phase 1, 78 IPS
242 progenitor cells and 391 normal MEFs are labeled; for phase 2, 84 IPS progenitor cells and

243 420 normal MEFs are labeled; for phase 3, 74 IPS progenitor cells and 370 normal MEFs are
244 labeled. Each of these three initial cell image sets are divided into the training and test sets:
245 70% of cell images for each time phases are selected randomly as training set with the
246 remainder (30%) as test set. The ratio between progenitor cell images and normal MEFs cell
247 images is kept approximately 1:5 for these training and testing sets. For the the training sets,
248 there are 55 iPS progenitor cells and 274 normal MEF cells in phase 1, 59 iPS progenitor cells
249 and 294 normal MEF cells in phase 2, as well as 52 iPS progenitor cells and 259 normal MEF
250 cells in phase 3.

251 In this paper, the initial cell dataset is used for cross-validating the proposed method, and
252 the training dataset is used for missing value processing and feature selection. For different
253 analytic steps, the specific data sample size depends on the time period from which the data
254 has been collected. Numerical features are calculated for all cell images in the datasets and
255 saved in CSV files. All datasets are standardized utilizing z-score.

256

257 **Missing values processing**

258 Processing missing values for the cells in the corresponding frames is an important step
259 for our model. Imaris cannot continuously identify all the cells in the frame due to different
260 parameter settings or complex three-dimensional cell environment. This implies that there
261 exists a certain number of cell images with missing feature values in the uniform time periods.
262 A certain number of missing images in the frames are permitted for cells to guarantee a
263 modest data size, and missing cell features are estimated with an imputation method. To
264 choose the most appropriate approach, we first analyze the impact of the number of missing

265 frames on the model, and then analyze the effect of three different imputation methods under
266 the corresponding missing frame numbers. Details for the three imputation methods are as
267 follows:

- 268 • *set_mean*. The missing value is set to the average value of all nonempty frames for a
269 specific type of feature in its sample from the selected time window.
- 270 • *set_KNN*. The missing value is set to the weighted average value of five nearest
271 nonempty neighbor frames for a specific type of feature in its sample. The calculation
272 of weight uses k-Nearest Neighbor (KNN) algorithm. The formula is as

$$273 \quad \text{Missing value}_{\text{frame}_i} = \sum_j w_{\text{frame}_j} \cdot \text{feature}_{\text{frame}_j}, w_{\text{frame}_j} = \frac{1}{\sqrt{(i-j)^2}} \quad (1)$$

274 where j represents the index of five nearest frames neighbor for missing frame i .

- 275 • *set_mean_mod*. Missing value is set to the average value of five nearest nonempty
276 neighbor frames for a specific type of feature in its sample.

277

278 **Time window and feature selection**

279 Because of the two rules used in dataset generation (Section **Cell image datasets**
280 **generation**), although images are provided up to 49 hours, it is unable to construct the model
281 based on the whole period. From a total of 49 hours, numerous time periods can be chosen,
282 and the model needs to select best time windows among all these eligible time periods. Time
283 window selection includes start frame selection and window length selection. Start frame
284 represents the moment that the time window starts from, and window length represents frame
285 number that the time window contains. For each time window with a selected time frame and
286 window length, we train and validate the proposed method on the corresponding dataset

287 generated. Validation is performed with 5-fold cross validation and the evaluation metric is
288 precision.

289 Morphological and motion feature selection is used to improve the performance. Since it
290 is difficult to guarantee image recording time to be accurately consistent for every batch
291 through experiments, model performance needs to be robust among wider time periods. Every
292 type of features contains multiple frames of features from the corresponding best time
293 windows. Features in a time window are treated as a bundle so we can learn the dynamic cell
294 growth process.

295 There are two steps for feature selection. The first step is recursive feature elimination.
296 Firstly, we use all 11 types of features to train the model with 5-fold cross validation and
297 calculate its precision as initial unimportance score. Then we delete each type of feature at a
298 time and obtain 11 precision values as new unimportance scores. We compare every new
299 score with the initial score, and remove the feature type with the largest unimportance score
300 higher than initial score. The recursive process will be repeated on feature set until the model
301 performance can be no longer improved or there is no feature. We then rank the importance of
302 all 11 types of features and delete the least important feature types. Second, we calculate the
303 Pearson correlation coefficient for the selected feature types from step 1 to remove the highly
304 correlated features with a correlation coefficient of 0.60 or above.

305

306 **Machine learning model and validation**

307 XGBoost, a Boosting algorithm, is used in this paper for feature selection and IPS cell
308 recognition. XGBoost integrates many weak tree-classifiers together to form a strong

309 classifier. This algorithm applies numerous strategies to prevent overfitting, and it is widely
310 utilized in data science such as cell analysis [39-43]. Hyperparameters of XGBoost are tuned
311 using grid-search for model training with selected features and best time windows.

312 For model validation, firstly we use 5-fold cross-validation on the initial cell image
313 datasets from the time windows of the three phases. Dataset generated from initial cell-sets
314 contains about 70 iPS cells for each phase. The ratio of iPS cells and normal MEFs keeps as
315 1:5 in each dataset.

316 In order to test the model's ability/robustness to predict the iPS progenitor cells around
317 the neighborhood of the corresponding training time window, holdout validation is performed.
318 Because iCD1 medium change is operated manually during the experiments, it is
319 impracticable to guarantee that for per batch data the duration of medium change is accurately
320 consistent with the existing data. This inconsistency might lead to a non-exact match between
321 the timeline after medium change and the timeline used in the model training process. The
322 holdout validation is designed as follows, for the model trained on time window $i \sim j$, we
323 examine the model's performance on several neighbor time windows, including time windows
324 $i-3 \sim j-3$, $i-2 \sim j-2$, $i-1 \sim j-1$, $i \sim j$, $i+1 \sim j+1$, $i+2 \sim j+2$, and $i+3 \sim j+3$, where i represents start
325 time frame of the window and j represents the terminal frame. The training dataset from time
326 window $i \sim j$ is generated from the initial training image data sets (70% of the initial total
327 dataset), and test datasets of the seven neighbor time windows are generated from the test
328 datasets (30% of the initial total dataset).

329 Moreover, in order to further test our model's ability to predict the iPS progenitor cell on
330 a time window which doesn't overlap with the window in the training process, an independent

331 test is performed. Model performance is tested on time windows which are far away from the
332 training time windows. Since we have three time phases, we first select test time windows in
333 phase 2 and 3 for the models trained on time windows of phase 1 and 2 respectively. For
334 testing our model developed for phase 3, we select the independent test time windows also in
335 phase 3, but without any overlap with the corresponding training time windows.

336

337 **Evaluation metrics**

338 In this paper, precision is mainly used for evaluation defined as,

$$339 \quad \textit{precision} = \frac{TP}{TP + FP}$$

340 where TP and FP represent the number of true positive and false positive prediction. This
341 metric evaluates the accuracy for the positive sample predicted by the model. Biologists need
342 a cell sample set enriched with true iPS progenitor cells so that in the early stage of
343 reprogramming progenitor cells can be studied with high probability.

344

345 **Results and Discussion**

346

347 **Missing frames processing and imputation method**

348 First, the effect of missing frames and imputation methods on the model's performance
349 was analyzed. Experiment for missing value was performed under six kinds of missing frame
350 numbers, which were numbers below or equal to five, four, three, two, one and zero. Model
351 performance was tested for each missing frame number with three imputation methods on
352 time periods of two window lengths (10 and 19 frames) located in three phases, which were

353 time period/window 19h30min ~ 21h10min from phase 1 (TP1), 25h50min ~ 27h30min from
354 phase 1 (TP2), 41h50min ~ 43h30min from phase 2 (TP3), 18h10min ~ 21h20min from phase
355 2 (TP4), 26h ~ 29h10min from phase 3 (TP5) and 42h ~ 45h10min from phase 3 (TP6).

356 Two window lengths (10 and 19 frames) were selected because a reasonable number of
357 continuous cell images could be traced. A short window will have more data but the motion
358 and morphological pattern of iPS progenitor cells cannot be learned while a long window will
359 result in a much smaller dataset. For each length, we chose three time windows randomly to
360 study whether different lengths would affect model performance under uniform missing frame
361 number. Datasets were generated from the training datasets, which were about 52~59 iPS
362 cells and 259~294 normal MEFs for time windows with 10 frames, 43~50 iPS cells and
363 238~264 normal MEFs for time windows with 19 frames. Model was evaluated by the
364 average precision with 5-fold cross validation over 20 times.

365 **Fig 2** showed the comparison results of different missing frame numbers and imputation
366 methods. For each missing number and imputation method, **Fig 2(a)** described the average
367 precision over six time windows (TP1 to TP6), indicated by blue boxes for set_KNN, red
368 boxes for set_mean and green boxes for set_mean_mod. Also shown in **Fig 2(a)** was the
369 average precision over all three imputation methods, indicated by grey boxes. **Fig 2(b)**
370 described the standard deviations of the corresponding precision values in **Fig 2(a)**. Detailed
371 precisions for all six time periods (TP1~TP6) were provided in Figure S1 of the **S1 File**.

372 **Fig 2. Model comparison for different missing frame number and imputation methods**

373 Fig 2(a) shows the average precision over six time periods (TP1 to TP6) for each missing
374 frame number and imputation method set_KNN (colored as blue), set_mean (colored as red),

375 set_mean_mod (colored as green) and all three imputation methods (colored as gray). Fig 2(b)
376 shows the standard deviation, as a function of missing frame number, of imputation method
377 set_KNN (colored as blue), set_mean (colored as red), set_mean_mod (colored as green) and
378 all three imputation methods (colored as gray).

379 **Fig 2(a)** showed that precision was higher when several missing frames were allowed.
380 For missing frame number of 0, the average precision of all method was only 0.585 and all
381 the average precisions of non-zero missing frame numbers were higher than 0.585. **Fig 2(a)**
382 also showed that the maximum average precision of all method was about 0.632 under
383 missing frames of 4, 4.7% higher than precision under no missing frames and 0.9% higher
384 than precision under missing frame number of 2. On one hand, the size of the dataset is larger
385 when missing value is permitted, on the other hand, the missing frame may introduce new
386 pattern for classification because iPS progenitor cells proliferate more frequently than normal
387 MEFs, and cell division can partly result in missing value. When cells divide at a certain
388 frame in their time periods, the feature values of all subsequent frames are missing.

389 In **Fig 2(b)**, the maximum standard deviation of all methods as indicated by gray box
390 was 0.061 under missing 4 frames. For each specific method, the maximum standard
391 deviation was 0.081 for Set_mean under 5 missing frames. The precision with two missing
392 frame numbers had the minimum standard deviation for all method (0.048 as indicated by
393 gray boxes) and at the same time it was also very close to the maximum precision (0.623
394 compared with the maximum value of 0.632 in **Fig 2(a)**). In addition, Set_mean_mod showed
395 the minimum standard deviation of all 3 imputation methods for all missing frame numbers
396 (indicated by green boxes), an indication of stable performance. Although Set_mean_mod

397 also showed smallest standard deviation for missing frame number of 1, its precision value of
398 missing frame number was smaller than that of missing frame number of 2. Therefore, we
399 used missing frame number less than or equal to two and select imputation method as
400 set_mean_mod in our model.

401

402 **Time window selection**

403 Time window selection was performed to select best time windows with high precision
404 for each phase. Since Imaris could not detect all cell images in every frame, the whole time
405 periods of three phases were divided into numerous time windows. For time window selection
406 (including start frame and window length), we set start frame to 21 time points which were
407 18h20min, 18h40min, 19h, 19h20min, 19h40min, 20h, 20h20min, 26h10min, 26h30min,
408 26h50min, 27h10min, 27h30min, 27h50min, 28h10min, 42h10min, 42h30min, 42h50min,
409 43h10min, 43h30min, 43h50min, 44h10min in three phases. Meanwhile, we set window
410 length to 12 different values including 7, 9, 11, 13, 15, 17, 19, 21, 23, 25, 27 and 29 frames.
411 For the total of 252 (12 times 21) time windows, we first generated datasets for each time
412 window with 11 types of morphological/motion features. All datasets were generated based
413 on the training dataset and contained about 38~59 iPS progenitor cells and about 190~295
414 normal MEFs. Then we selected the optimal time window through 5-fold cross-validation
415 based on 20 XGBoost runs.

416 The model performance on these different time windows was shown in **Fig 3**. In this
417 figure, shorter window lengths were marked in red colors and longer window lengths were
418 marked in blue colors. We observed that precision of longer window lengths was lower than

419 that of shorter window lengths in three phases, and this trend was less pronounced for phase 3.
420 The size of the dataset may be the major reason for this trend. Due to the two rules in dataset
421 generation, the amount of samples satisfying conditions decreases gradually with the
422 increasing window length. For window length of 29 frames, there are just about 38 iPS
423 progenitor cells and 262 normal MEFs in phase 1, about 44 iPS progenitor cells and 283
424 normal MEFs in phase 2, about 36 iPS progenitor cells and 242 normal MEFs in phase 3. As
425 compared with the window length of 7 frames, there are about 53 iPS progenitor cells and 290
426 normal MEFs in phase 1, about 55 iPS progenitor cells and 285 normal MEFs in phase 2,
427 about 57 iPS progenitor cells and 300 normal MEFs in phase 3. On the other hand, the
428 number of samples is much less for later start frame than that for previous time since some
429 cells have divided. For instance, there are only about 30 iPS progenitor cells and 200 normal
430 MEFs for the last start frame with length of 29 frames in phase 3.

431 **Fig 3. Time window selection**

432 The three subplots represent the precision values for different time windows based on 21 start
433 frames (x axis) and 12 window lengths (7 frames to 29 frames) for phases 1, 2, and 3 (from
434 top to bottom) respectively, and the black dash line in each subplot indicates a precision value
435 of 0.55.

436 Selection of best time windows according to maximum precision resulted in an unstable
437 prediction performance. For instance, precision achieved the maximum value on the time
438 window starting at 43h30min with length of 29 frames while all its adjacent time windows
439 had poor performance with lower precision. It is unlikely to achieve the same performance on
440 a new dataset of the same time window.

441 We selected the best start frame for each phase respectively. To exclude the start frame
442 with high prediction precision for only 1 or 2 window lengths, 14 candidates of best start
443 frames were selected when precision was above 0.55 for at least three successive window
444 lengths. For each candidate best start frame, the average precision was calculated over the
445 successive window lengths whose precision was above 0.55 and the average precision values
446 were shown above each candidate best start frame in **Fig 3**. We only selected one best start
447 frame for each phase according to the average precision values of the candidate best start
448 frames, resulted in 19h40min, 26h10min and 42h30min for phases 1, 2 and 3, respectively.

449 Secondly, the candidate best window lengths were selected whose precision values were
450 all above 0.55 for 3 best start frames of step 1, resulting in window lengths 11, 13, 15 and 17
451 frames. For each window length, the precision values, average precisions and the
452 corresponding standard deviation of 3 different best start frames were provided in Table S1 of
453 **S1 File**. The average precision of 0.640 for window length of 13 frame was the highest while
454 its standard deviation was the smallest (0.01), thus window length of 13 frames was selected
455 as the best window length.

456

457 **Two-step feature selection**

458 We performed a two-step feature selection method on three phases respectively. Firstly,
459 we generated datasets from best time windows based on the training cell image datasets. The
460 dataset of each phase contained 11 types of morphological and motion features, all of which
461 contained about 50~59 iPS progenitor cells and about 200~295 normal MEFs.

462 For the first step, an iterative feature removal procedure was performed on the

463 corresponding dataset of each phase to study the importance of each feature type. Average
464 precision was calculated via 5-fold cross-validation over 20 runs on the dataset of each phase,
465 and later sets as initial unimportance score. Next, we removed each type of features and
466 calculated the unimportance scores (average precision). Feature with maximum score would
467 be deleted only if this score was greater than the initial unimportance score, which would then
468 be updated as the maximum score. This step was repeated until no score was greater than
469 initial score or no more feature could be selected.

470 Results from step 1 feature selection were shown in **Fig 4**. For phase 1 precision was no
471 longer improving after removing ellipsoid-oblate, displacement and volume; for phase 2
472 precision was no longer improving after removing displacement and volume; for phase 3
473 precision was no longer improving after removing displacement, ellipsoid-prolate, area and
474 volume. In the end, eight types of features were selected for phase 1, nine types of features
475 were retained for phase 2, and seven types of features were retained for phase 3. Selected
476 features from this step were indicated in **Fig 4** by star symbols. The corresponding precisions
477 for best windows with 13 frames before feature selection were 0.624, 0.607, 0.646 for phases
478 1, 2 and 3, respectively, and after feature selection, these precision values had increased to
479 0.691, 0.613 and 0.682 respectively.

480 **Fig 4. Feature ranking and selection**

481 This figure shows how the precision values change with the deleted feature in a recursive
482 fashion. Least important features are removed earlier.

483 The removing order of feature type in **Fig 4** indicated the importance of each feature
484 type. We observed from **Fig 4** that three types of features, nucleus-cytoplasm ratio, sphericity

485 and intensity-StdDev, were important among all three phases. Nucleus-cytoplasm ratio was
486 the top important factor in three phases. Sphericity and intensity-StdDev were among the top
487 4 common features of three phases. Intensity showed clear different patterns between normal
488 MEFs and progenitor cells. As shown in **Fig 5(a)**, the progenitor cells in the blue circles
489 showed a uniform intensity distribution between nucleus and cytoplasm, while for normal
490 MEFs in the yellow boxes, the cytoplasm showed weaker intensity as indicated by the
491 blurring edges. Also shown in **Fig 5(a)**, the nucleus and cytoplasm of progenitor cells in the
492 blue circles and normal MEFs in the yellow boxes were enlarged and colored by light blue
493 and green respectively. It is clear that nucleus-cytoplasm ratio for progenitor cells are much
494 larger than that of normal MEFs. From **Fig 5(a)**, the cell area of progenitor cells is also
495 smaller on average than normal MEFs, indicating the importance of sphericity since area is
496 closely related to sphericity by the equation from Part 1 of the **S1 File**. The selected features
497 are consistent with the experimental results that iPS progenitor cells exhibit higher
498 nucleus-cytoplasm ratio, smaller total area, and higher proliferation rate than normal
499 MEFs[21].

500 **Fig 5. iPS progenitor cells vs. MEFs and Feature correlation**

501 (a) shows the examples of iPS progenitor cell images (blue circles) and normal MEFs images
502 (yellow boxes) taken from phase 1, 2 and 3 of field 2 (Left, middle and right). Nucleus and
503 cytoplasm of the enlarged progenitor cells and normal MEFs are colored in light blue and
504 green respectively. (b) shows the Pearson coefficients between remaining types of features in
505 three phases after the first step of feature selection. Note in this figure ellipsoid-prolate is
506 denoted as E-prolate, intensity-StdDev as I-stdDev, intensity-min as I-Min, intensity-max as

507 I-Max, nucleus-cytoplasm volume ratio as Ratio, ellipsoid-oblate as E-oblate.

508 In order to further study the correlations of different features, as a second step we
509 calculated the Pearson correlation coefficients between the selected features. The results for
510 three phases were shown in **Fig 5(b)**. In our model, two feature types were considered
511 strongly correlated if the coefficient was greater than 0.6 and one of them was removed.
512 When two different feature types were strongly correlated with a third feature type, both of
513 them were removed with the purpose of keeping as less number of features as possible. For
514 phase 1, the coefficient between sphericity and area was 0.77 in phase 1, and the coefficient
515 between sphericity and ellipsoid-prolate was 0.66, thus area and ellipsoid-prolate were
516 removed from the list. Similarly, they were removed for phase 2 as well. The strong
517 correlation between sphericity, ellipsoid-prolate and area is caused by the fact that Imaris
518 extracts features from two-dimensional cell images assuming cell thickness as constant.
519 Furthermore, since ellipsoid-oblate was associated with cell thickness, it was removed from
520 the feature list as well for phase 2 and phase 3. Overall, six types of features (Sphericity,
521 I-Min, I-stdDev, I-Max, Ratio, Speed) were selected for all the models.

522

523 **Cross-validation**

524 With selected features, a grid-search scheme was used for hyperparameter optimization
525 of XGBoost with 5-fold cross-validation, and the datasets were generated based on the
526 training sets for three phases. Three hyperparameters such as `learning_rate`, `n_estimators` and
527 `gamma` were set to 0.01, 385 and 0 respectively. We had validated our model with three
528 different experiments as shown in **Fig 1**.

529 For cross-validation, datasets were generated from initial whole cell image dataset.
530 Dataset for phase 1 contained about 63 iPS progenitor cells and about 326 normal MEFs.
531 Dataset for phase 2 contained about 82 iPS progenitor cells and about 427 normal MEFs.
532 Dataset for phase 3 contained about 72 iPS progenitor cells and about 359 normal MEFs. For
533 each phase, 5-fold cross validation was performed 10 times on every best time windows with
534 6 selected feature types, resulting in a total of 117 for window length of 13 frames. **Fig 6(a)**
535 showed precision scores for 3 different phases, and all of the precision values were above
536 0.580. For phase 1, the precision value was highest, 0.732.

537 **Fig 6 Model validation**

538 In all sub-figures, X axis indicates the start frame of the best time windows and the
539 corresponding window length (13 frames) is indicated in the inlet. (a) 5-fold cross-validation
540 precisions over 10 runs. (b) the standard deviation of the average precision of the
541 neighborhood time windows in Figure 6(d). (c) the standard deviation of the average
542 precision of the distant windows in Figure 6(e). (d) the average precision of seven
543 neighborhood time windows calculated over 10 holdout validation runs. (e) the average
544 precision over 10 independent tests for six best time windows on their corresponding distant
545 windows.

546

547 **Holdout validation**

548 Holdout validation was used to test the model's ability to predict the iPS progenitor cells
549 in the neighborhood of the time window in which the model had been trained. Since in real
550 application, it is difficult to generate the dataset whose images have the exact start time as in

551 the training dataset, holdout-validation is very important for testing the model's generality on
552 the neighborhood time windows. For each phase, the training dataset for window length of 13
553 frames was generated. In phase 1, the window start frame I was 19h40min as shown in **Fig**
554 **6(d)**. Models trained on this dataset was then tested on seven test datasets corresponding to
555 start frames I, I-1, I-2, I-3, I+1, I+2 and I+3, illustrated in **Fig 1** and **Fig 6(d)**. There was no
556 overlap between the training and testing datasets.

557 For each time window, average precision value was computed over 10 holdout validation
558 runs, and the results were shown in **Fig 6(d)**. The minimum average precision values were
559 0.616 for window length of 13 frames and start frame I-2 in phase 1, 0.522 for window length
560 of 13 frames and start frame I-2 in phase 2 and 0.566 for window length of 13 frames and
561 start frame I-3 in phase 3. These minimum precisions were all smaller than the corresponding
562 precisions in **Fig 6(a)**; what is more, **Fig 6(d)** also showed the average precision values for
563 phase 1, 2 and 3 were all smaller than the cross-validation resulted in **Fig 6(a)**, indicating the
564 difficulties for predicting the neighborhood time windows.

565 For each result of the 3 phases in **Fig 6(d)**, the standard deviations of average precisions
566 were computed for window length of 13 frames in **Fig 6(b)**. The maximum deviation was
567 0.042 for window length of 13 frames in phase 1 and this indicated the trained models were
568 relatively stable in terms of prediction precision in a wide range of neighborhood windows.

569

570 **Independent test**

571 Finally, to test the model's ability to predict the iPS progenitor cells on a distant time
572 window without overlapped frames with the training window, we performed an independent

573 test. If the training cell trajectory is long and contains enough typical iPS progenitor cells, the
574 trained model on one window should be able to identify the motion and morphological
575 patterns of iPS progenitor cells against normal MEFs, regardless of the selected time window.

576 For phase 1, the model trained on time window 19h40min~21h40min (length of 13
577 frames) was tested on time windows of phase 2, including time windows starting from
578 26h20min (S11), 26h40min (S12), 27h (S13), 27h20min (S14), 27h40min (S15), and 28h
579 (S16), shown in the first panel of **Fig 6(e)**. Similarly, for phase 2, the model trained on time
580 windows 26h10min~28h10min (length of 13 frames) was tested on six time windows of
581 phase 3 starting from 42h10min (S21), 42h30min (S22), 42h50min (S23), 43h10min (S24),
582 43h30min (S25), 43h50min (S26), shown in the middle panel of **Fig 6(e)**. Lastly, for phase 3,
583 model testing was performed on the distant time windows without overlapped frames from
584 the same phase, shown in the right panel of **Fig 6(e)**. For time windows 42h30min~44h30min,
585 we selected test time windows starting from 45h10min (S31), 45h30min (S32), 45h50min
586 (S33), 46h10min (S34), 46h30min (S35).

587 Results of the independent test runs were shown in **Fig 6(e)**. The minimum precision was
588 0.523 for window length of 13 frames for S16 in phase 1. The average precision of phase 1
589 was lower than those of holdout validation and cross-validation, however, the average
590 precision of phase 2 and 3 were both better than cross-validation and holdout validation. For
591 the prediction of distant time windows, our model could have worse performance than that of
592 neighborhood windows, but our model could also outperform the cross validation and holdout
593 validation (indicated by the standard deviation in **Fig 6(c)**). The reason was the independent
594 test datasets for phase 2 and 3 were closely related to the training dataset. The standard

595 deviations of the independent tests were much higher than those of the holdout validation,
596 which could also be seen from the large fluctuations of the precision values in **Fig 6(e)**.
597 Nevertheless, the minimum average prediction precision was above 52% among all the
598 experiments, and maximum average precision was about 0.750 for the independent test in
599 phase 3.

600

601 **Conclusion**

602 In this paper, we proposed a machine learning based model together with time-lapse
603 image analysis to predict/identify iPS progenitor cells during the first 3-5 days after
604 reprogramming initiation. The model generated a variety of morphological and motion
605 features among different time windows, then relied on a two-step feature selection algorithm
606 to select the most important features. The proposed computational approach is very unique
607 from previous experimental techniques which identify the iPS progenitor cells by
608 retrospectively tracking the cell images manually frame by frame from the image frame of
609 GFP expression.

610 By the experimental study of the enriched iPS progenitor cells in the early stage of
611 reprogramming, the proposed method could provide a new technique or attempt for
612 experimenters to improve the iPS reprogramming efficiency and to study the underlying
613 mechanism of iPS reprogramming. Morphological and motion features, especially sphericity,
614 intensity-StdDev and nucleus-cytoplasm volume ratio, have been found most important for
615 the progenitor cell classification, which is consistent with the experimental observations.

616 Cross-validation of the proposed method trained and tested on the same time window

617 showed that the prediction precision is above 0.580 for all three phases. Since in real
618 applications, it is very difficult to match imaging timeline precisely between different
619 experiments, holdout validation and an independent test are also performed to test the model's
620 ability to predict iPS progenitor cells in the neighborhood time windows and distant time
621 windows, respectively. The results showed our model can predict the iPS progenitor cells
622 with a minimum precision of 52% for neighborhood windows and distant windows, and the
623 maximum average precision is about 0.750 for the independent test in phase 3. The prediction
624 performance of our model tends to have a larger fluctuation for distant windows than for
625 neighborhood windows, indicated by the larger standard deviation of independent test runs.

626 For future works, models on different time windows for each phase can be combined to
627 achieve higher prediction accuracy.

628

629 **Acknowledgment**

630 This work is supported by the National Key Research and Development Program of
631 China under Grant No. 2016YFB0201305 and 2018YFB0204403; National Science
632 Foundation of China under grant no. U1435215 and 61433012; the Shenzhen Basic Research
633 Fund under grant no. JCYJ20160331190123578, JCYJ20170413093358429 and
634 GGF2017073114031767; Chinese Academy of Sciences grant under no. 2019VBA0009.

635 We would also like to thank the funding support by the Shenzhen Discipline Construction
636 Project for Urban Computing and Data Intelligence, Youth Innovation Promotion Association,
637 CAS to Yanjie Wei.

638

640 Reference

- 641 1. Takahashi K, Yamanaka S. Induction of pluripotent stem cells from mouse embryonic and adult
642 fibroblast cultures by defined factors. *Cell*. 2006;126(4):663-76.
- 643 2. Yamanaka S. Induced pluripotent stem cells: past, present, and future. *Cell Stem Cell*.
644 2012;10(6):678-84.
- 645 3. Takayama N, Nishimura S, Nakamura S, Shimizu T, Ohnishi R, Endo H, et al. Transient
646 activation of c-MYC expression is critical for efficient platelet generation from human induced
647 pluripotent stem cells. *J Exp Med*. 2010;207(13):2817-30.
- 648 4. Nori S, Okada Y, Yasuda A, Tsuji O, Takahashi Y, Kobayashi Y, et al. Grafted human-induced
649 pluripotent stem-cell-derived neurospheres promote motor functional recovery after spinal cord injury
650 in mice. *Proc Natl Acad Sci U S A*. 2011;108(40):16825-30.
- 651 5. Okamoto S, Takahashi M. Induction of retinal pigment epithelial cells from monkey iPS cells.
652 *Invest Ophthalmol Vis Sci*. 2011;52(12):8785-90.
- 653 6. Kriks S, Shim JW, Piao J, Ganat YM, Wakeman DR, Xie Z, et al. Dopamine neurons derived
654 from human ES cells efficiently engraft in animal models of Parkinson's disease. *Nature*.
655 2011;480(7378):547-51.
- 656 7. Israel MA, Yuan SH, Bardy C, Reyna SM, Mu Y, Herrera C, et al. Probing sporadic and familial
657 Alzheimer's disease using induced pluripotent stem cells. *Nature*. 2012;482(7384):216-20.
- 658 8. Ben-David U, Benvenisty N. The tumorigenicity of human embryonic and induced pluripotent
659 stem cells. *Nat Rev Cancer*. 2011;11(4):268-77.
- 660 9. Kanemura H, Go MJ, Shikamura M, Nishishita N, Sakai N, Kamao H, et al. Tumorigenicity
661 studies of induced pluripotent stem cell (iPSC)-derived retinal pigment epithelium (RPE) for the
662 treatment of age-related macular degeneration. *PLoS One*. 2014;9(1):e85336.
- 663 10. Okita K, Ichisaka T, Yamanaka S. Generation of germline-competent induced pluripotent stem
664 cells. *Nature*. 2007;448(7151):313-7.
- 665 11. Sridharan R, Tchiew J, Mason MJ, Yachechko R, Kuoy E, Horvath S, et al. Role of the murine
666 reprogramming factors in the induction of pluripotency. *Cell*. 2009;136(2):364-77.
- 667 12. Shu J, Wu C, Wu Y, Li Z, Shao S, Zhao W, et al. Induction of pluripotency in mouse somatic
668 cells with lineage specifiers. *Cell*. 2013;153(5):963-75.
- 669 13. Cacchiarelli D, Trapnell C, Ziller MJ, Soumillon M, Cesana M, Karnik R, et al. Integrative
670 Analyses of Human Reprogramming Reveal Dynamic Nature of Induced Pluripotency. *Cell*.
671 2015;162(2):412-24.
- 672 14. He X, Cao Y, Wang L, Han Y, Zhong X, Zhou G, et al. Human fibroblast reprogramming to
673 pluripotent stem cells regulated by the miR19a/b-PTEN axis. *PLoS One*. 2014;9(4):e95213.
- 674 15. Huh S, Song HR, Jeong GR, Jang H, Seo NH, Lee JH, et al. Suppression of the ERK-SRF axis
675 facilitates somatic cell reprogramming. *Exp Mol Med*. 2018;50(2):e448.
- 676 16. Miles DC, de Vries NA, Gisler S, Lieftink C, Akhtar W, Gogola E, et al. TRIM28 is an
677 Epigenetic Barrier to Induced Pluripotent Stem Cell Reprogramming. *Stem Cells*. 2017;35(1):147-57.
- 678 17. Polo JM, Anderssen E, Walsh RM, Schwarz BA, Nefzger CM, Lim SM, et al. A molecular
679 roadmap of reprogramming somatic cells into iPS cells. *Cell*. 2012;151(7):1617-32.
- 680 18. Dabiri Y, Gama-Brambila RA, Taskova K, Herold K, Reuter S, Adjaye J, et al. Imidazopyridines
681 as Potent KDM5 Demethylase Inhibitors Promoting Reprogramming Efficiency of Human iPSCs.
682 *iScience*. 2019;12:168-81.

- 683 19. Hong H, Takahashi K, Ichisaka T, Aoi T, Kanagawa O, Nakagawa M, et al. Suppression of
684 induced pluripotent stem cell generation by the p53-p21 pathway. *Nature*. 2009;460(7259):1132-5.
- 685 20. Robertson A, Mohamed TM, El Maadawi Z, Stafford N, Bui T, Lim DS, et al. Genetic ablation of
686 the mammalian sterile-20 like kinase 1 (Mst1) improves cell reprogramming efficiency and increases
687 induced pluripotent stem cell proliferation and survival. *Stem Cell Res*. 2017;20:42-9.
- 688 21. Smith ZD, Nachman I, Regev A, Meissner A. Dynamic single-cell imaging of direct
689 reprogramming reveals an early specifying event. *Nat Biotechnol*. 2010;28(5):521-6.
- 690 22. Zhang J, Nuebel E, Daley GQ, Koehler CM, Teitell MA. Metabolic regulation in pluripotent stem
691 cells during reprogramming and self-renewal. *Cell Stem Cell*. 2012;11(5):589-95.
- 692 23. Li R, Liang J, Ni S, Zhou T, Qing X, Li H, et al. A mesenchymal-to-epithelial transition initiates
693 and is required for the nuclear reprogramming of mouse fibroblasts. *Cell Stem Cell*. 2010;7(1):51-63.
- 694 24. Megyola CM, Gao Y, Teixeira AM, Cheng J, Heydari K, Cheng EC, et al. Dynamic migration
695 and cell-cell interactions of early reprogramming revealed by high-resolution time-lapse imaging. *Stem
696 Cells*. 2013;31(5):895-905.
- 697 25. Dufour A, Thibeaux R, Labruyere E, Guillen N, Olivo-Marin JC. 3-D active meshes: fast discrete
698 deformable models for cell tracking in 3-D time-lapse microscopy. *IEEE Trans Image Process*.
699 2011;20(7):1925-37.
- 700 26. Dzyubachyk O, van Cappellen WA, Essers J, Niessen WJ, Meijering E. Advanced level-set-based
701 cell tracking in time-lapse fluorescence microscopy. *IEEE Trans Med Imaging*. 2010;29(3):852-67.
- 702 27. Maska M, Danek O, Garasa S, Rouzaut A, Munoz-Barrutia A, Ortiz-de-Solorzano C.
703 Segmentation and shape tracking of whole fluorescent cells based on the Chan-Vese model. *IEEE
704 Trans Med Imaging*. 2013;32(6):995-1006.
- 705 28. Türetken E, Wang X, Becker CJ, Haubold C, Fua P. Network Flow Integer Programming to Track
706 Elliptical Cells in Time-Lapse Sequences. *IEEE Transactions on Medical Imaging*. 2017;36(4):942-51.
- 707 29. Payer C, Štern D, Neff T, Bischof H, Urschler M, editors. Instance Segmentation and Tracking
708 with Cosine Embeddings and Recurrent Hourglass Networks. *Medical Image Computing and
709 Computer Assisted Intervention – MICCAI 2018*; 2018 2018//; Cham: Springer International
710 Publishing.
- 711 30. Erdmann G, Volz C, Boutros M. Systematic approaches to dissect biological processes in stem
712 cells by image-based screening. *Biotechnol J*. 2012;7(6):768-78.
- 713 31. Van Valen DA, Kudo T, Lane KM, Macklin DN, Quach NT, DeFelice MM, et al. Deep Learning
714 Automates the Quantitative Analysis of Individual Cells in Live-Cell Imaging Experiments. *PLoS
715 Comput Biol*. 2016;12(11):e1005177.
- 716 32. Chen CL, Mahjoubfar A, Tai LC, Blaby IK, Huang A, Niazi KR, et al. Deep Learning in
717 Label-free Cell Classification. *Sci Rep*. 2016;6:21471.
- 718 33. Kraus OZ, Grys BT, Ba J, Chong Y, Frey BJ, Boone C, et al. Automated analysis of high-content
719 microscopy data with deep learning. *Mol Syst Biol*. 2017;13(4):924.
- 720 34. Gao Z, Wang L, Zhou L, Zhang J. HEp-2 Cell Image Classification With Deep Convolutional
721 Neural Networks. *IEEE J Biomed Health Inform*. 2017;21(2):416-28.
- 722 35. Stumpf PS, MacArthur BD. Machine Learning of Stem Cell Identities From Single-Cell
723 Expression Data via Regulatory Network Archetypes. *Front Genet*. 2019;10:2.
- 724 36. Chen T, Guestrin C. XGBoost: A Scalable Tree Boosting System. *Proceedings of the 22nd
725 ACM SIGKDD International Conference on Knowledge Discovery and Data Mining - KDD '16*2016.
726 p. 785-94.

- 727 37. Chen J, Liu J, Chen Y, Yang J, Chen J, Liu H, et al. Rational optimization of reprogramming
728 culture conditions for the generation of induced pluripotent stem cells with ultra-high efficiency and
729 fast kinetics. *Cell Res.* 2011;21(6):884-94.
- 730 38. Esteban MA, Wang T, Qin B, Yang J, Qin D, Cai J, et al. Vitamin C enhances the generation of
731 mouse and human induced pluripotent stem cells. *Cell Stem Cell.* 2010;6(1):71-9.
- 732 39. Aibar S, González-Blas CB, Moerman T, Huynh-Thu VA, Imrichova H, Hulselmans G, et al.
733 SCENIC: single-cell regulatory network inference and clustering. *Nature Methods.* 2017;14:1083.
- 734 40. Li H, Pang F, Shi Y, Liu Z. Cell dynamic morphology classification using deep convolutional
735 neural networks. *Cytometry A.* 2018;93(6):628-38.
- 736 41. Zhong J, Sun Y, Peng W, Xie M, Yang J, Tang X. XGBFEMF: An XGBoost-Based Framework
737 for Essential Protein Prediction. *IEEE Trans Nanobioscience.* 2018;17(3):243-50.
- 738 42. Chen CLP, Zhang T, Chen L, Tam SC. I-Ching Divination Evolutionary Algorithm and its
739 Convergence Analysis. *IEEE Transactions on Cybernetics.* 2017;47(1):2-13.
- 740 43. Zhang T, Chen CLP, Chen L, Xu X, Hu B. Design of Highly Nonlinear Substitution Boxes Based
741 on I-Ching Operators. *IEEE Transactions on Cybernetics.* 2018;48(12):3349-58.

742

743 **Supporting information**

744 **S1 File. Supplementary Material**

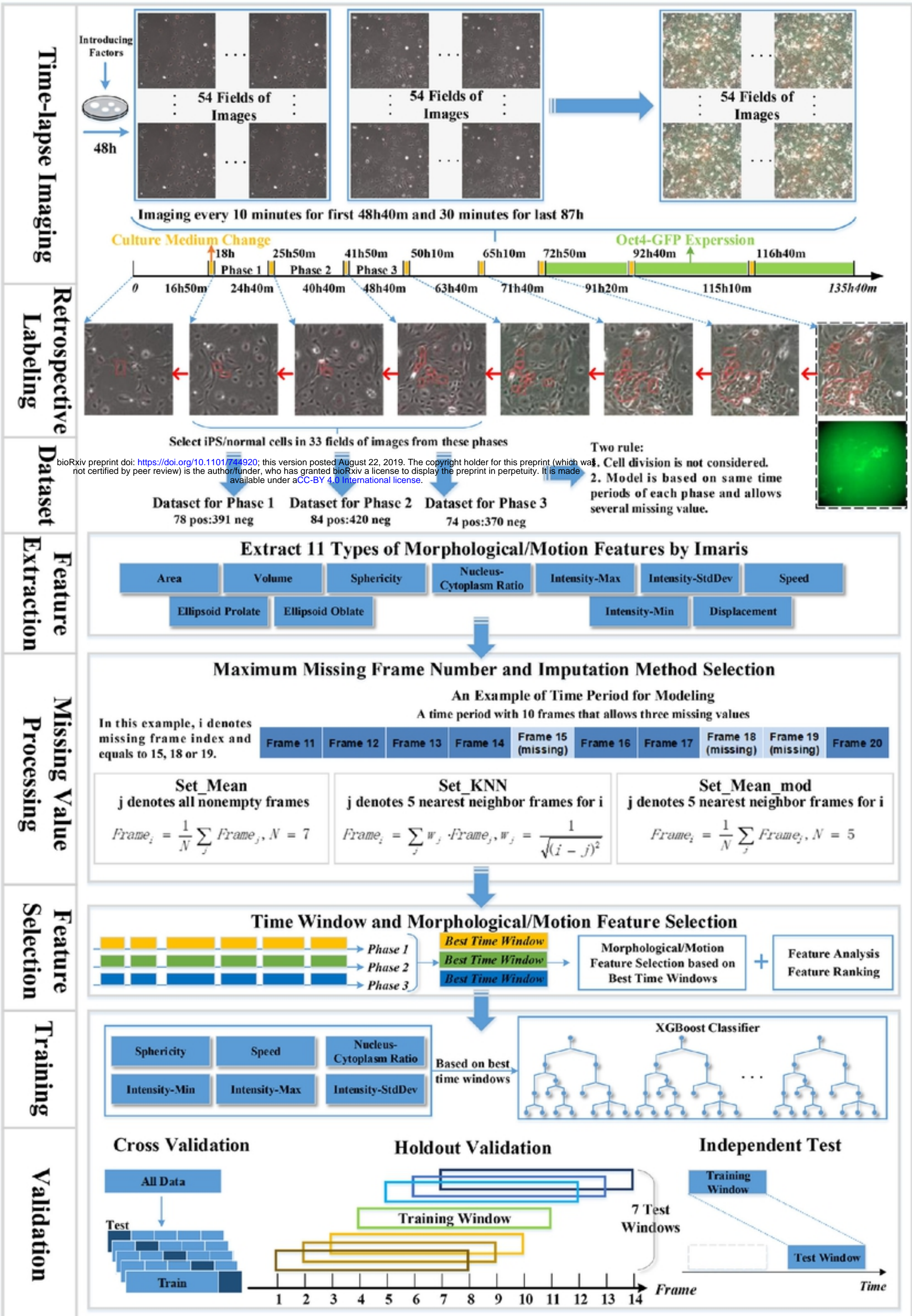


Fig 1

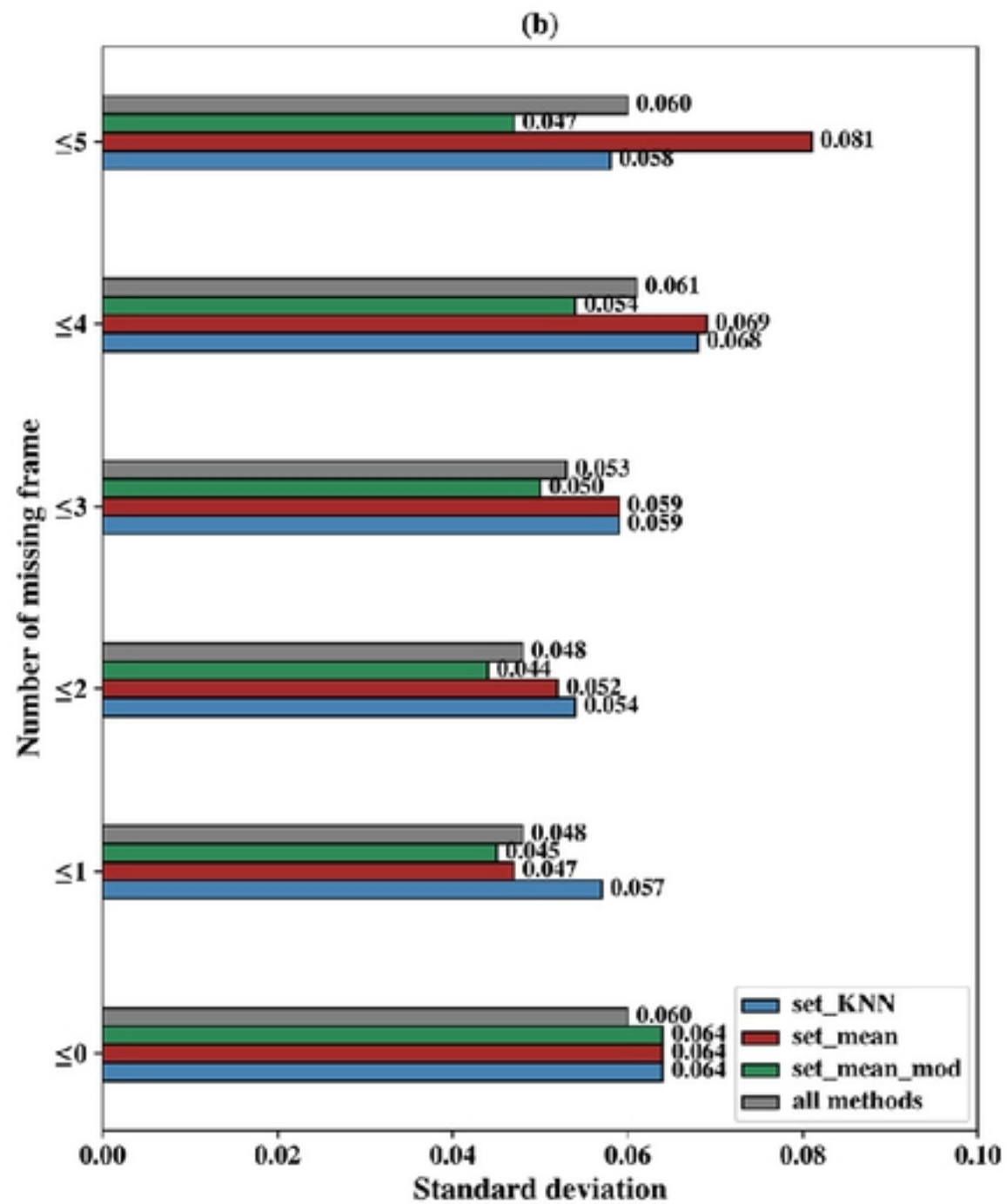
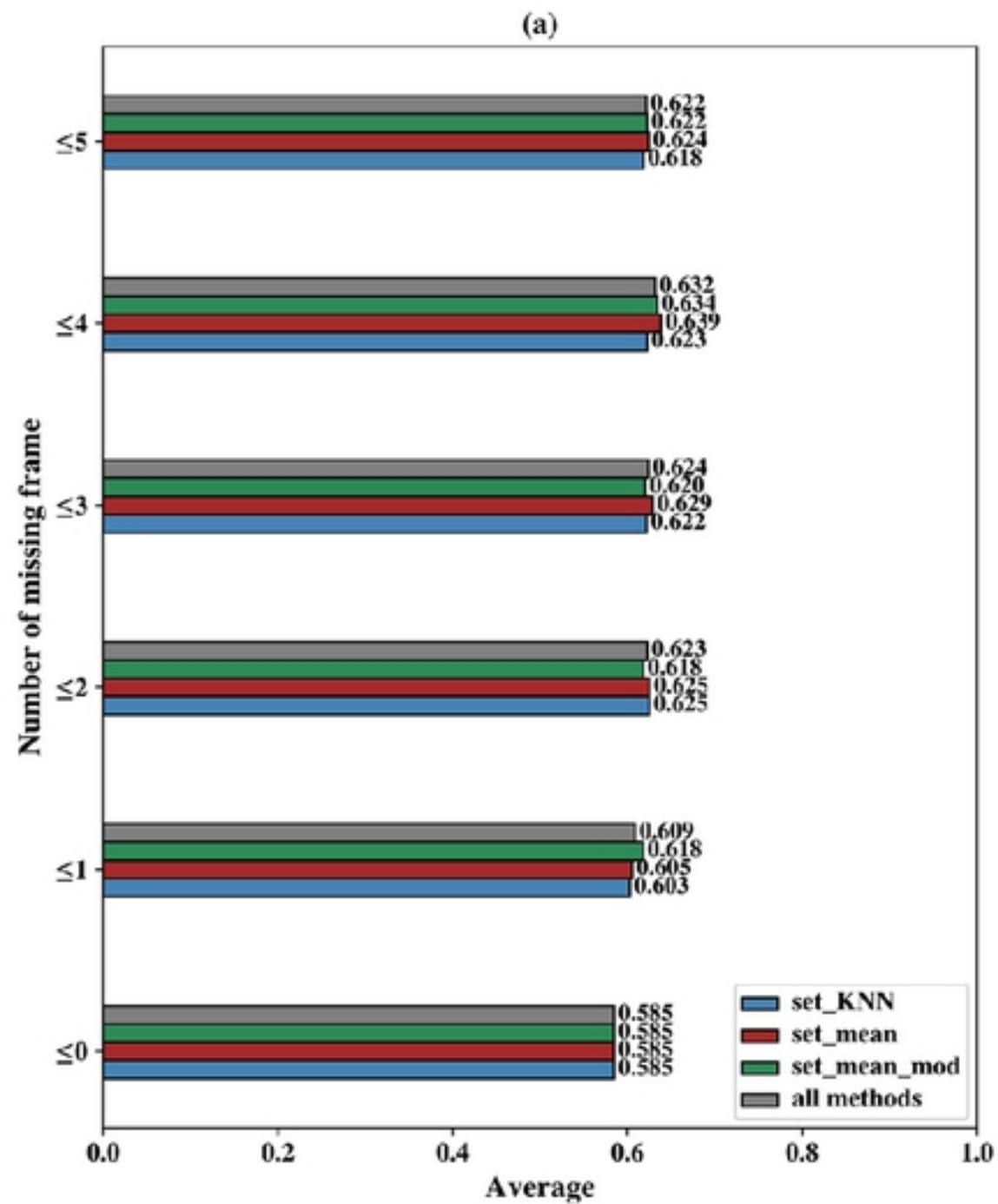


Fig2

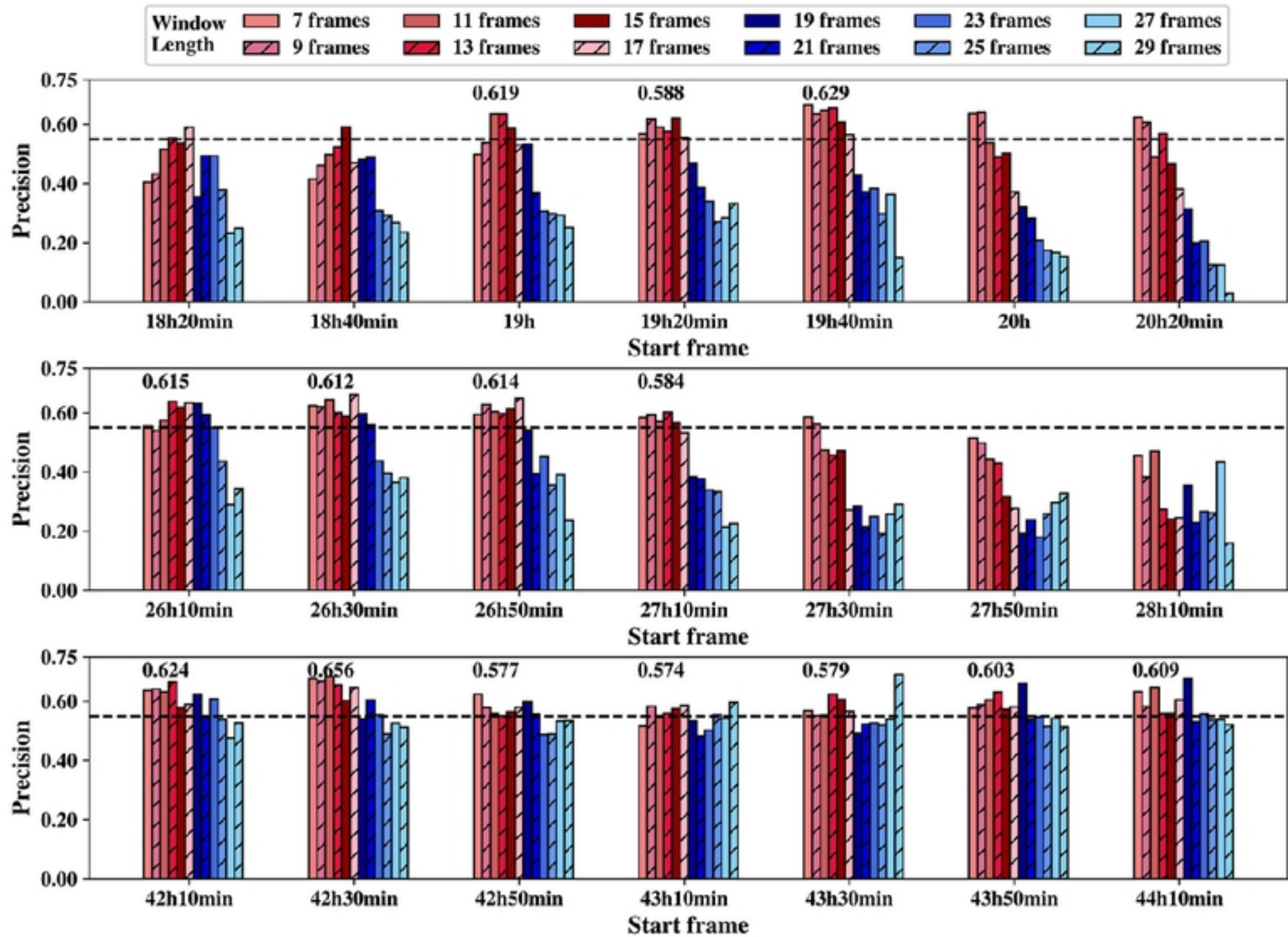


Fig3

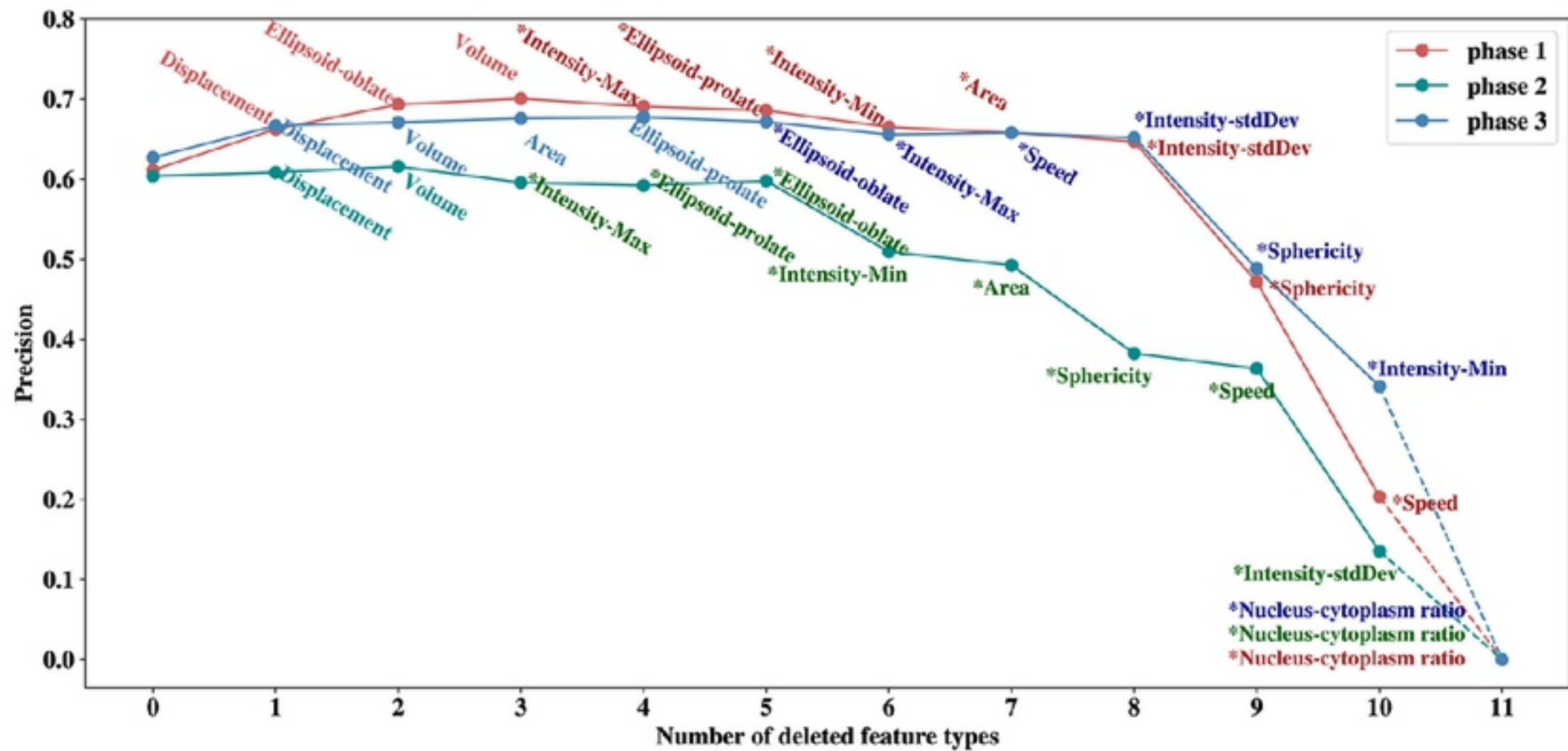
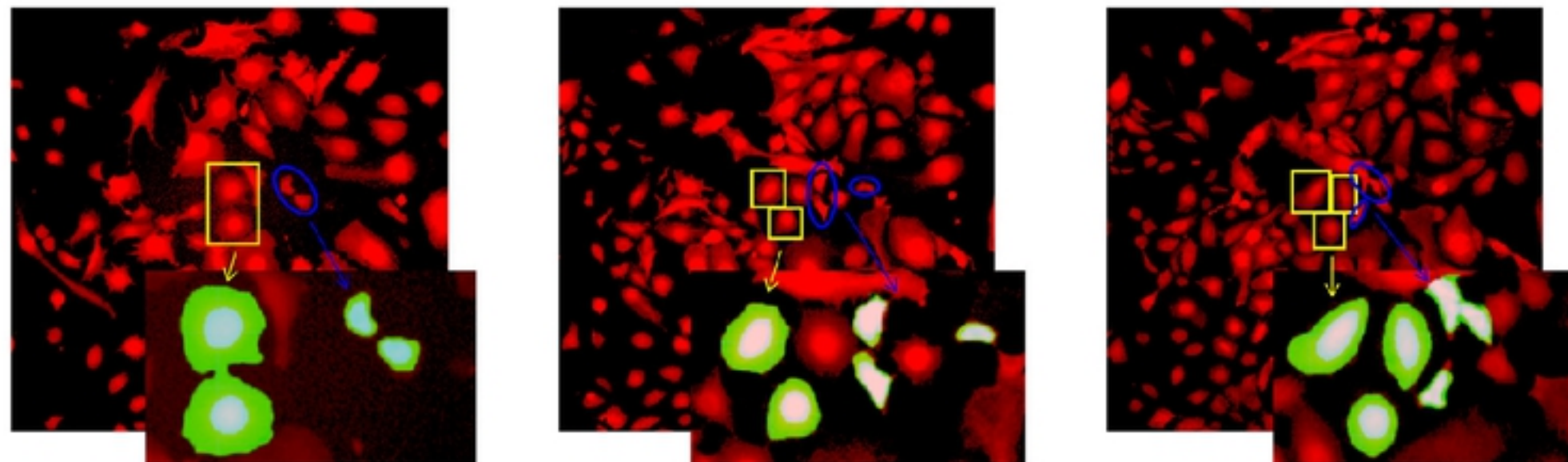


Fig4

(a)



(b)

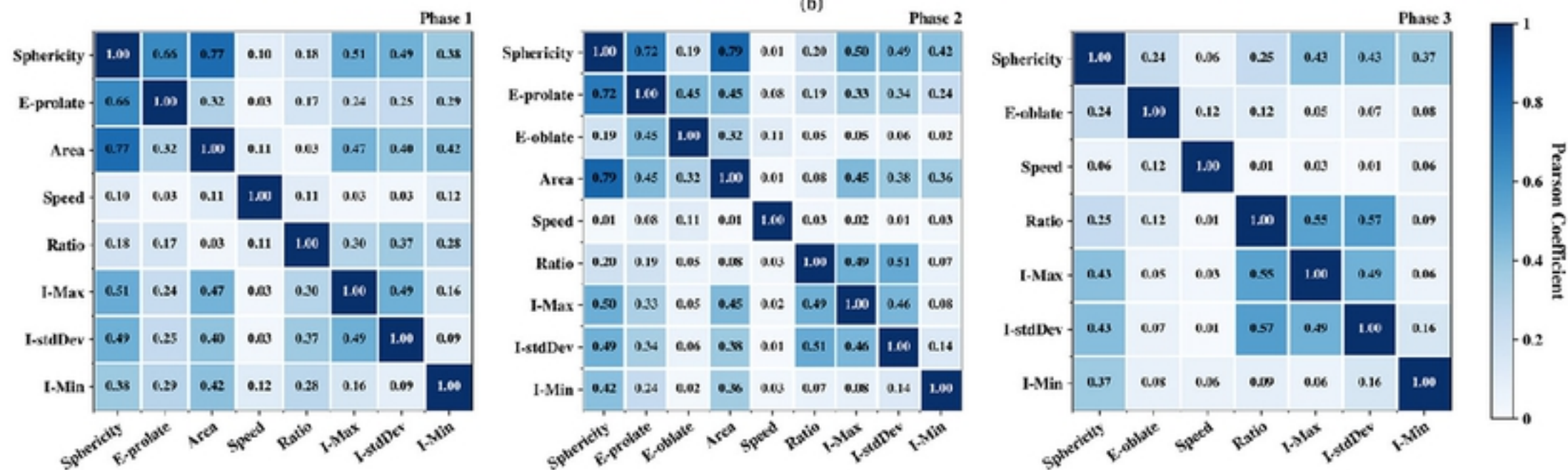


Fig5

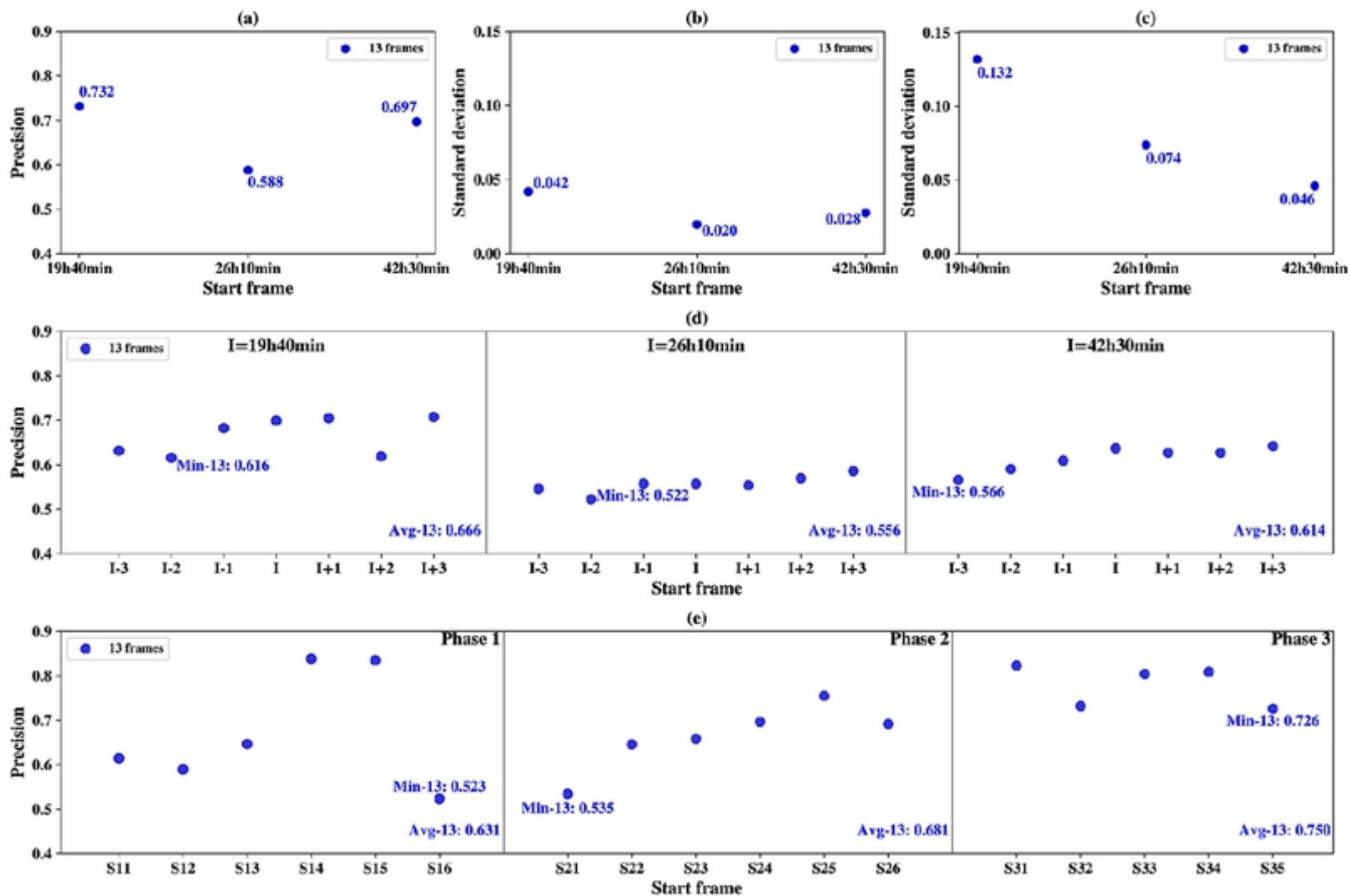


Fig6